

1 **Cellular-scale silicon probes for high-density, precisely-localized neurophysiology.**

2  
3 Daniel Egert<sup>1</sup>, Jeffrey R Pettibone<sup>1</sup>, Stefan Lemke<sup>2</sup>, Paras R. Patel<sup>3</sup>, Ciara M. Caldwell<sup>3</sup>,  
4 Dawen Cai<sup>4</sup>, Karunesh Ganguly<sup>1,5,6</sup>, Cynthia A. Chestek<sup>3,7,8,9</sup>, Joshua D. Berke<sup>1,6</sup>.

5  
6 1) Department of Neurology, University of California, San Francisco.

7 2) Neuroscience Graduate Program, University of California, San Francisco.

8 3) Department of Biomedical Engineering, University of Michigan, Ann Arbor.

9 4) Department of Molecular and Cell Biology, University of Michigan, Ann Arbor.

10 5) Veterans Affairs Medical Center, San Francisco.

11 6) Weill Institute for Neurosciences and Kavli Institute for Fundamental Neuroscience, University of  
12 California, San Francisco.

13 7) Department of Electrical Engineering and Computer Science, University of Michigan, Ann Arbor.

14 8) Neurosciences Program, University of Michigan, Ann Arbor.

15 9) Robotics Program, University of Michigan, Ann Arbor.

16  
17  
18 **Corresponding Author:** Joshua Berke, Department of Neurology, 675 Nelson Rising Lane, CA 94143, USA.  
19 [joshua.berke@ucsf.edu](mailto:joshua.berke@ucsf.edu)

20  
21 **Author Contributions:**

22 Conceptualization: DE, JDB; Methodology: DE, JRP; Formal Analysis: DE; Investigation: DE, SL, PRP, CMC,  
23 JRP; Writing – Original Draft: DE, JDB; Supervision: JDB, CAC, KG; Funding Acquisition: JDB, CAC, KG.

24  
25 **Running Head:** Cellular-scale silicon probes.  
26

27 **Abstract:**

28 Neural implants with large numbers of electrodes have become an important tool for examining brain  
29 functions. However, these devices typically displace a large intracranial volume compared to the neurons they  
30 record. This large size limits the density of implants, provokes tissue reactions that degrade chronic performance,  
31 and impedes the ability to accurately visualize recording sites within intact circuits. Here we report next-  
32 generation silicon-based neural probes at cellular-scale (5x10 $\mu$ m cross-section), with ultra-high-density packing  
33 (as little as 66 $\mu$ m between shanks) and 64 or 256 closely-spaced recording sites per probe. We show that these  
34 probes can be inserted into superficial or deep brain structures and record large spikes in freely behaving rats for  
35 many weeks. Finally, we demonstrate a slice-in-place approach for the precise registration of recording sites  
36 relative to nearby neurons and anatomical features, including striatal  $\mu$ -opioid receptor patches. This scalable  
37 technology provides a valuable tool for examining information processing within neural circuits, and potentially  
38 for human brain-machine interfaces.

39

40

41 **New and Noteworthy:**

42 Devices with many electrodes penetrating into the brain are an important tool for investigating neural  
43 information processing, but they are typically large compared to neurons. This results in substantial damage, and  
44 makes it harder to reconstruct recording locations within brain circuits. This paper presents high-channel-count  
45 silicon probes with much smaller features, and a method for slicing through probe, brain, and skull all together.  
46 This allows probe tips to be directly observed relative to immunohistochemical markers.

47

48

49 **Keywords:**

50 Microelectrodes; High-density recording; Neural circuits; Striatum.

51

## 52 Introduction

53 Much of our current understanding of neural functions was gained through electrophysiological recording  
54 from individual neurons in behaving animals, one-at-a-time. Yet recording neurons one-at-a-time provides only a  
55 very limited view of information processing, which involves rapid interactions and coordination between neurons  
56 (Fujisawa *et al.* 2008). Simultaneous recordings from ensembles of many neurons has been achieved using large  
57 numbers of wires (Schwarz *et al.* 2014), microfabricated electrode grids (e.g. the Utah array; Mitz *et al.* 2017), or  
58 microelectrode arrays shaped through photolithography (Berényi *et al.* 2014; Jun *et al.* 2017; Merriam *et al.* 2011;  
59 Scholvin *et al.* 2016; Shobe *et al.* 2015). These important approaches have yielded valuable results, but  
60 nonetheless share substantial limitations, especially for investigating densely-packed, locally-connected neurons.

61 To achieve the stiffness needed for a millimeters-long element to penetrate the brain, each element has  
62 typically had a width of at least 25-100 $\mu\text{m}$  (with cross-section in the thousands of  $\mu\text{m}^2$ ). This large foreign body  
63 causes substantial direct mechanical damage, and is also detected and rejected by the brain's immune system  
64 (Biran *et al.* 2005; Potter *et al.* 2012; Prasad *et al.* 2012; Saxena *et al.* 2013; Winslow and Tresco 2010). The  
65 immune reaction leads to loss of neurons in the vicinity of the electrodes, one factor that frequently curtails the  
66 duration of chronic neural recordings (Patel *et al.* 2016). The spacing between large elements must also be large to  
67 distribute tissue damage - for example, in a standard Utah array contacts are separated by 400 $\mu\text{m}$ . For many brain  
68 regions and cell types, this means that the neurons monitored from different electrodes are unlikely to be in direct  
69 communication with each other (Fujisawa *et al.* 2008; Straub *et al.* 2016).

70 Compounding this problem, large devices must be removed from the brain before processing the tissue  
71 for histological analysis. Since the recording electrodes are not observed *in situ*, it has proven difficult to obtain  
72 accurate registration between electrophysiological recordings and key anatomical markers. Lack of anatomical  
73 registration has impeded research in several subfields, including the investigation of the function of striatal  
74 "patches" (irregularly-shaped,  $\sim 100\mu\text{m}$ -scale zones that are detectable through staining for mu-opioid receptors,  
75 a.k.a. striosomes; Desban *et al.* 1993; Graybiel *et al.* 1981). Although visualization of spatial patterns of ensemble  
76 activity can be achieved through other methods - such as multiphoton imaging of genetically-encoded calcium  
77 indicators - these currently lack the exquisite temporal resolution of electrophysiology (though see Adam *et al.*  
78 2019).

79 Several approaches have been used to insert smaller electrodes into the brain. For example, flexible,  
80 cellular-scale electrodes can be infused through a micropipette (Liu 2018) and linear polymer probes can be  
81 dragged into the brain using a stiff needle or silicon support as a shuttle (Chung *et al.* 2019; Hanson *et al.* 2019).  
82 However these insertion devices are typically at least as large as traditional electrodes (25 $\mu\text{m}$ + in width; though  
83 see Luan *et al.* 2017). The resulting acute "stab-wound" has been shown to cause substantial, permanent neuron  
84 loss even if no foreign body remains in the brain (Potter *et al.* 2012). As an alternative, very thin (<10 $\mu\text{m}$ )  
85 electrodes made from carbon fibers can be directly inserted, either one at a time (Kozai *et al.* 2012), in bundles  
86 (Guitchounts *et al.* 2013) or mounted on silicon supports to increase overall stiffness and penetration (Patel *et al.*

87 2015). The latter approach shows promising chronic performance (Patel *et al.* 2016), but has not yet demonstrated  
88 the feasibility of large channel counts.

89 To overcome these limitations, we designed neural probes with high channel counts but considerably  
90 smaller physical shank dimensions than standard silicon devices. We reasoned that the force required to insert an  
91 element without buckling depends on its length; by coupling a relatively short (500 $\mu\text{m}$ ) electrode-bearing lower  
92 portion with cellular-scale cross-section (5x10 $\mu\text{m}$ ) to a more robust upper portion (far from the recording sites),  
93 we obtained reliable insertion even deep into the brain. The smaller size probes allow much higher density neural  
94 recording, with excellent chronic performance for months (at least) after implant. We further developed a method  
95 whereby probes are left in place during brain sectioning and histological processing, by slicing through the entire  
96 head after decalcifying the skull. This was made possible by the very thin probe shanks that can be easily sliced  
97 through without distorting the surrounding tissue. By cutting thick ( $\sim$ 300 $\mu\text{m}$ +) slabs of tissue and using  
98 immunohistochemistry to detect key anatomical features, we found that we can directly visualize identified  
99 recording sites within intact micro- and meso-scale neural circuits.

## 100 **Methods and Materials.**

### 101 **Nanofabrication process flow and probe assembly**

102 The probes were fabricated at the Lurie Nanofabrication Facility at the University of Michigan. The  
103 process begins with thermally growing and patterning a 1.2 $\mu\text{m}$  thick oxide on a silicon wafer as a masking layer.  
104 A 20 $\mu\text{m}$  deep and 1.2 $\mu\text{m}$  wide trench is etched using DRIE (deep reactive ion etching) where stiffeners are  
105 placed. The etch recipe was optimized to achieve vertical side-walls and high aspect ratio trenches. Boron is  
106 thermally diffused at 1175 $^{\circ}\text{C}$ , 12 $\mu\text{m}$  deep into silicon surface in places that were not masked. The mask is  
107 removed except for a small section around the probe tip ends. A second, 5 $\mu\text{m}$  shallow boron diffusion is  
108 performed to define the thickness of the tips. A stack of electrically insulating silicon oxide and silicon nitride is  
109 deposited using low pressure chemical vapor deposition. A 1.4 $\mu\text{m}$  thick layer of electrically conductive,  
110 phosphorous-doped polysilicon is deposited and patterned to form interconnects. For this step, patterns formed by  
111 stepper and e-beam lithography (for 256-channel probes) are stitched together. The e-beam was only used to keep  
112 the narrow traces separate. The polysilicon traces routing along the tip of the probes were designed to have a  
113 470nm minimum feature size. Another stack of insulators (identical to those previously mentioned) is deposited.  
114 After etching vias, Cr/Pt/Au is sputtered and patterned via lift-off to form bonding pads and electrodes. Lastly, the  
115 outline of the probe is defined using DRIE, and any undoped silicon is wet etched in EDP (ethylenediamine  
116 pyrocatechol). For handling and protection of the fine tips, the devices remain attached to the wafer frame by  
117 small tabs. The probes were mounted onto printed circuit boards (PCBs) using Crystalbond 509 (SPI supplies)  
118 and wire bonded.

119 **Animal surgery**

120 All animal procedures were approved by the Institutional Animal Care and Use Committees at the University of  
121 Michigan and the University of California, San Francisco. The probes were implanted into adult male Long-Evans  
122 rats, weighing 300 – 350g. Anesthesia was initialized with 5% isoflurane (v/v). The rats were maintained under  
123 isoflurane anesthesia, which was continuously monitored using toe pinch and breathing rate, and the flow of  
124 isoflurane was adjusted accordingly. The head was shaved at and around the area of the incision site. The shaved  
125 area was swabbed using alternating applications of betadine and 70% ethanol. Ointment was applied to the eyes to  
126 keep them from drying during surgery. Ear bars were mounted in both ears and fixed in a stereotaxic frame (Kopf  
127 Instruments, Model 900). After making an incision, the skin flaps were pulled apart using hemostats and the skull  
128 surface was cleaned using cotton swabs and 2% hydrogen peroxide (v/v). A burr bit (19008-07, Fine Science  
129 Tools, Foster City, CA) was used to drill holes around the periphery of the skull for bone screws (19010-00, Fine  
130 Science Tools, Foster City, CA). Reference and ground wires originating from the implant were attached to bone  
131 screws using MillMax pins and placed 1mm caudal to lambda and over the contralateral cerebellum, respectively.  
132 Next, a 2x4mm craniotomy was made over the target brain region. The dura was gently resected using dural  
133 forceps and hook, and insertion was performed within minutes of resection to avoid excessive swelling. Special  
134 care was taken to avoid larger blood vessels on the surface of the brain and if necessary, specific shanks were  
135 broken off. Just before the probe tips contacted the surface of the brain, excess liquid was removed in order to  
136 prevent shanks from wicking together. Shanks were lowered at about 100  $\mu\text{m/s}$  into the brain. Striatal shanks were  
137 lowered to  $\sim 4.2$  mm below the surface of the brain, leaving  $\sim 800$   $\mu\text{m}$  shank length above the brain surface. Motor  
138 cortical shanks were lowered  $\sim 1.5$ mm below the surface (at +0.5AP, 3.5ML relative to bregma). For the cohort of  
139 rats used for chronic stability testing, and the pallidal implant, the exposed surface of the brain was sealed with  
140 Kwik-Sil (World Precision Instruments, Sarasota, FL; Patel *et al.* 2015). The motor cortex implant was sealed  
141 with cyanoacrylate glue (Loctite SuperGlue Gel control). The rat implanted in striatum for slice-in-place was  
142 sealed with a thin layer of DOWSIL (3-4680, Dow Corning, Midland, MI) and petroleum jelly (Vaseline) coated  
143 along the shanks (Jun *et al.* 2017). Finally, the skull was covered with dental acrylic (Hygenic Acrylics,  
144 Switzerland).

145 **Recordings, impedance measurements**

146 PCBs with 64 channel probes were connected to RHD2216 64-channel headstages, and PCBs with 256-channel  
147 probes were connected to two RHD2000 128-channel headstages (Intan Technologies, Los Angeles, USA). In  
148 some cases these connections were made using custom flexible polyimide cables (MicroConnex / Carlisle  
149 Interconnect, USA), consisting of 30 $\mu\text{m}$  copper trace/spaces, sandwiched between 25 $\mu\text{m}$  thick polyimide layers,  
150 with bonding pads plated with immersion gold. Recordings were made using the Intan interface software (version  
151 1.5.2). The sampling rate was 30 kS/s for the striatal implants, 25 kS/s for the GP implant and 20 kS/s for the  
152 motor cortex implant. The sample depth was always 16-bit. Semi-automated clustering was performed using  
153 KiloSort2 (Pachitariu *et al.* 2016) followed by manual curation using the ‘phy’ gui

154 (<https://github.com/kwikteam/phy>). Impedances (at 1kHz) were measured using the Intan headstages. For  
155 assessment of spiking across repeated sessions, we examined brief (10 min) epochs as rats were resting quietly.  
156 Signals were first subjected to common average referencing, then high-pass filtered at ~234Hz using a wavelet  
157 transform (Wiltschko *et al.* 2008). In line with prior studies (Jun *et al.* 2017), spike events were detected using a  
158 threshold of 6x median absolute deviation of the signal, with 0.5ms dead time between possible spikes. To  
159 prevent contributions from occasional large movement artifacts, portions of the filtered signal that crossed a 1mV  
160 threshold were discarded, as were spike events that fell within a millisecond window in which the mean amplitude  
161 across all channels was more than 3x the average for the whole session. Analyses did not include channels that  
162 were not connected to brain (impedance outside the range 500-4000 kOhm) due to mechanical failure (e.g.  
163 detachment of connector pins after multiple plug-in, plug-out cycles). We estimated the physical location of  
164 recorded single-units in each of two dimensions, by finding the peaks of Gaussians fit to average peak spike  
165 amplitudes across the electrodes (averaged along, or across, shanks, respectively).

### 166 **Slice-in-place, histology and imaging**

167 Rats were transcardially perfused with 4% paraformaldehyde (PFA) in phosphate buffered saline (PBS). After  
168 perfusion, the rats were decapitated, the skull was stripped of gross tissue, and the jaw was removed. The  
169 remaining bone, brain and probes were immersed in a solution of 0.25M tetra-sodium ethylenediaminetetraacetic  
170 acid (EDTA) in PBS, pH-balanced to 7.4. The solution was exchanged daily, with the soak continuing for 2-3  
171 weeks until the bone turned rubbery. The skulls were soaked in 30% sucrose in PBS for 72hrs for cryoprotection,  
172 then the solution was progressively exchanged with OCT (optimal cutting temperature compound). Once the  
173 sample was immersed in 100% OCT, it was brought into a vacuum to facilitate penetration into ventricles then  
174 frozen using dry ice. Slicing was performed on a cryostat at -16°C. The skull was mounted such that the most  
175 ventral portion was accessed first. The tissue was sliced together with the bone and the probes, at 300µm  
176 thickness. The resulting slabs were washed, blocked and incubated for 7-10 days at room temperature with both  
177 primary antibodies Rb  $\alpha$  mOR (ImmunoStar 24216) and Ms  $\alpha$  NeuN (Millipore MAB377). The slabs were then  
178 incubated with secondary antibodies for 3-5 days at 4°C. Before imaging on a confocal microscope (Nikon TI),  
179 the slabs were soaked in a refractive index matching agent (TDE; Staudt *et al.* 2007). The obtained images were  
180 processed using ImageJ.

181

## 182 **Results.**

### 183 **Neural probe design**

184 Each device consists of 32 shanks in a comb-like configuration (Fig. 1). Each shank has an electrode-  
185 bearing tip section (500µm long) with cellular-scale cross-section (10µm wide x 5µm thin). We designed multiple  
186 probe variations, in which each shank has lengths of 3-9mm, and holds two or eight electrode sites (64 or  
187 256 total channels / probe). Recording sites were 15µm x 10µm, and separated by 15µm gaps. Adjacent shanks

188 differ in length by 50 $\mu$ m to reduce peak insertion force. To enable insertion, probes have a wider upper portion,  
189 with 25 $\mu$ m width and 11.5 $\mu$ m thickness. For 6mm and 9mm long shanks, this upper portion widens gradually to  
190 40 $\mu$ m at the top.

## 191 **Nanofabrication Process**

192 The shanks were formed from the bulk of silicon wafers, and the interconnects, electrodes and insulators  
193 were patterned thin films deposited onto the wafers (Fig. 2). Materials and processing steps were derived from the  
194 Michigan probes process (Tanghe *et al.* 1990) which uses diffusion of boron into silicon to form etch stops and  
195 pattern the probe shape. Each probe design used one or more of the following technical refinements:

196 First, we patterned very high-density traces within the tip sections via electron-beam lithography, which  
197 allows for orders-of-magnitude smaller features (Du *et al.* 2011) compared to optical patterning. As e-beam  
198 lithography is a serial and thus relatively expensive process, we used it only on the lower, thin tip sections of 256-  
199 channel devices, to define the narrow valleys separating traces. The remaining traces were patterned using  
200 conventional optical stepper lithography.

201 Second, we integrated a stiffener into upper shank sections by selectively increasing thickness there  
202 (6mm, 9mm shank versions only). Traditionally in this process, neural probes have a uniform thickness defined  
203 by the depth of diffused boron in silicon. Here, a trench was etched along parts of the shank before boron  
204 diffusion. The sidewalls and the bottom of the trenches were exposed during boron doping and hence the  
205 thickness of this part of the shank is extended by the depth of the trench (increasing maximum thickness to  
206 30 $\mu$ m). The trenches were kept sufficiently narrow such that they were completely refilled in subsequent steps.

207 Third, we produced sharper tips by masking boron diffusion towards the end of the shank (3mm shank  
208 version only). Increasing tip sharpness can reduce compression of the brain during insertion and make buckling of  
209 the shanks less likely (Bjornsson *et al.* 2006). By masking boron diffusion at the very tip, the thickness of the  
210 released probe was reduced to that of the remaining insulating layers, around only 1.5 $\mu$ m.

## 211 **Successful implantation into shallow and deep brain structures**

212 After wire-bonding to custom PCBs, each finalized probe design was found to successfully insert into  
213 brain without requiring specialized surgical practices. During the design stage of this project, test probes (5mm  
214 length, not all shanks present) were inserted to a depth of several mm into the motor cortex of an anesthetized rat,  
215 then withdrawn. Successful insertion was defined as shanks remaining intact without obvious deflection from a  
216 straight path. Test probes without stiffeners were found to insert with some difficulty (n=2 test probes, 26/28 and  
217 16/28 shanks successfully inserted). Adding stiffeners and the tapering increase in top section width made  
218 insertion noticeably easier (n=2 test probes, 30/31 and 30/31 shanks successfully inserted).

219 Fig. 3A shows images of inserted devices with 3mm long shanks, with an extremely narrow pitch of  
220 66 $\mu$ m during implantation 1.5mm deep into rat cortex. We were also able to insert multiple devices, mounted on

221 thin flexible polyimide cables (see Methods), into the same hemisphere, targeting both motor cortex with a 6mm  
222 probe and striatum with a 9mm probe (Fig. 3B). Once inserted, the probes were secured, the site was sealed (see  
223 Methods), and rats consistently recovered from surgery (Fig. 3C) without behavioral impairments.

## 224 **Recording from large neuronal populations**

225 We successfully implanted 256-channel devices into brain structures both superficial (motor cortex) and  
226 deep (striatum, globus pallidus (GP)), and obtained high-quality chronic spike recordings in freely-moving rats  
227 from each structure. Fig. 4A shows an example from a 9mm, 256-channel probe targeting GP (3 days post-  
228 surgery), yielding 259 distinct simultaneously-recorded single-unit clusters.

229 The dense electrode arrangement both within- and between- shanks allows examination of the spatial  
230 extent of extracellular voltage changes associated with action potentials from each neuron. In our GP example  
231 (using 100 $\mu$ m shank pitch), each averaged action potential was visible only across a small number of recording  
232 sites (Fig. 4B). This is consistent with relatively small extracellular fields generated by these neurons, which  
233 typically have radially-symmetric dendritic fields (Kita and Kita 1994). By contrast, when we recorded from  
234 motor cortex (using a probe with just 66 $\mu$ m shank pitch), each averaged action potential was readily visible across  
235 many sites. This includes both sites along a shank (consistent with recording along the large apical dendrite;  
236 Blanche *et al.* 2005) and across two or even three shanks (Fig. 4C). This suggests that – at least for recording  
237 cortical projection neurons - our probes have sufficient density to detect spikes from a large proportion of cells  
238 within the two-dimensional field of recording sites.

## 239 **High-density, chronic spike recordings**

240 The cellular-scale silicon probes were capable of recording large spikes over extended time periods: Fig.  
241 5A shows an example recording at 139 days post-implant. To quantify changes in chronic performance over time  
242 we recorded from a cohort of rats (n=4) each with a 64-channel probe implanted in dorsal striatum, at 1 week and  
243 7 weeks post-implant (Fig. 5B).

244 We saw a slight decline (from 55.8 to 52.0, out of 64) in the mean number of working electrodes (defined  
245 as those with impedances between 0.5 and 4.0M $\Omega$ ); the remaining sites showed reduced impedance (mean per  
246 device fell from 2.2M $\Omega$  to 1.6M $\Omega$ ; mean per site from 2.2M $\Omega$  (n=225) to 1.5M $\Omega$  (n=211); two-  
247 tailed Wilcoxon signed-rank test, p=1.3e-19). The mean rate of spike events increased (per device: from 47Hz to  
248 60Hz threshold crossings/s/device; per site: from 0.8Hz (n=225) to 1.2Hz/s (n=211); two-tailed Wilcoxon signed-  
249 rank test for sites recorded at both timepoints, p=0.0481). The size of detected spikes was stable (mean per device,  
250 87.0 $\mu$ V to 85.4 $\mu$ V; mean per site 84.0 $\mu$ V (n=225) to 83.0 $\mu$ V (n=211); no change in size for those recorded at both  
251 timepoints; two-tailed Wilcoxon signed-rank test, p=0.2425). We conclude that these devices are able to  
252 consistently record spikes over many weeks.

253 **Anatomical registration of implanted probes *in situ*.**

254 To facilitate registration between recording sites and microcircuit features, we wished to avoid pulling  
255 electrodes out of the brain at the end of experiments, and instead leave electrodes *in situ* during processing for  
256 histology. Many standard electrodes (e.g. tetrodes or tungsten wires) cannot be cut through by cryostat blades  
257 without extensive tissue damage (J.R.P. and J.D.B, unpublished observations). Some recent electrode designs can  
258 be cut through (Xie *et al.* 2015) but do not preserve the orderly arrangement of electrodes needed for registration  
259 between specific recording channels and histological locations.

260 We found that – following formaldehyde perfusion and decalcification of the skull – we can cleanly cut  
261 through skull, brain, and probe shanks of rats with implanted cellular-scale silicon probes (Fig. 6A,B). By cutting  
262 300 $\mu$ m slabs we could directly observe the electrode-bearing portion of the shank tips within brain tissue (Fig.  
263 6B,C), while still allowing antibodies against  $\mu$ -opioid receptors (MOR) to fully penetrate the tissue and reveal  
264 striatal patches (Fig. 6D). Co-staining for the neuronal marker NeuN revealed many neuronal cell bodies  
265 immediately adjacent to probe tips, even after prolonged chronic implantation (Fig. 6E), consistent with minimal  
266 damage to local circuits. In 3-D confocal stacks we could identify the specific depth of shank tips (Fig 6F), and  
267 thereby reconstruct the positions of electrodes that recorded single-units, relative to the complex patch shapes (Fig  
268 6F,G). This slice-in-place approach thus allows effective direct visualization of electrodes within intact brain  
269 circuits.

270 **Discussion.**

271 We have demonstrated that silicon probes with cellular-scale tip sections can yield long-lasting chronic  
272 spike recordings in freely-moving animals, large numbers of densely-recorded neurons, and direct visualization of  
273 probe tips relative to histological markers. This combination of features is likely to be very useful for many  
274 systems neuroscience studies, especially investigations of neural circuit functions over a range of spatial scales.

275 Probes with very thin shanks are likely to produce less damage and improved localization compared to  
276 alternative advanced silicon probe designs, which have typically emphasized large numbers of sites on wider  
277 shanks (e.g. Blanche *et al.* 2005; Jun *et al.* 2017; Rios *et al.* 2016; Wang *et al.* 2019). Those designs may  
278 nonetheless have advantages for some applications, such as when multiple targets are arranged vertically within  
279 the brain (Jun *et al.* 2017). In other situations, such as recording from a horizontal cell layer, the current design  
280 may be more appropriate. The current design is suitable for a range of vertebrate species of mouse size and greater  
281 (e.g. all 256 recording sites will fit within the mouse striatum) but future design variations could readily expand  
282 the range of potential targets.

283 Neural probes made using flexible polymer substrates (Chung *et al.* 2019; Felix *et al.* 2013; Luan *et al.*  
284 2017; Xie *et al.* 2015) can also produce recordings with high longevity. Furthermore, their mechanical flexibility  
285 prevents breaking, and they may also be sliced-in-place (Dai *et al.* 2018). However, their insertion often requires  
286 transient mechanical support within the brain by removable shuttles (Chung *et al.* 2019; Musk and Neuralink

287 2019), that cause acute (stab-wound) damage and hinder narrow spacing between shanks. Once implanted,  
288 flexible devices cannot be further moved (Michon *et al.* 2016), preventing adjustments based on observed  
289 electrophysiological features after recovery, or recording of new sets of cells. Further advantages of silicon  
290 include the sophisticated assembly tools developed for silicon technology, and the potential to seamlessly include  
291 active electronics, for example for multiplexed readout (Jun *et al.* 2017), or LEDs for optical stimulation (Wu *et*  
292 *al.* 2015).

293 An alternative technology for recording many neurons simultaneously is optical imaging. This can have  
294 several important advantages including direct observation of neuron locations, visualization of distinct neuronal  
295 compartments (such as dendrites; Adam *et al.* 2019), or wide fields-of-view (Garg *et al.* 2019). However, imaging  
296 of large numbers of neurons has to date typically examined superficial structures in head-fixed animals, with  
297 calcium fluctuations detected by GCaMP as the activity measure. Calcium dynamics can have a non-  
298 straightforward relationship to spiking, and action potentials remain the gold standard measure of neural  
299 “activity”. Imaging action potentials is possible using voltage sensors instead (Adam *et al.* 2019) but the light  
300 intensity requirements for imaging at near-millisecond resolution make large fields of view impractical with  
301 current sensors. Recording from deep brain structures in freely moving animals has been made possible using  
302 miniaturized microscopes and gradient refractive index lenses (Cai *et al.* 2016). However these lenses are  
303 typically 0.5-2mm in diameter, and implantation involves aspirating overlying brain structures, potentially  
304 altering neural dynamics.

305 We deliberately placed recording electrodes far from the relatively thicker, stiffer shank portions, which  
306 presumably provoke greater tissue reactions. How far away is far enough? For solid silicon probes with 300 $\mu\text{m}$   
307 width and 15 $\mu\text{m}$  thickness, Skousen *et al.* (2011) showed that after 2 months neural density is low in the  
308 immediately adjacent vicinity, but is normal at 100 $\mu\text{m}$  distance. In the present design the closest recording site is  
309 250 $\mu\text{m}$  away from the thicker section (for 256-channel devices; 430 $\mu\text{m}$  away for 64-channel devices). We saw no  
310 indication that the electrodes further away from the tip (and thus closer to the thicker sections) record fewer  
311 neurons (Fig. 5A), suggesting that we have achieved sufficient distance from any damage caused by thicker upper  
312 sections. Although the aggregate cross-section of our recording tip sections is substantial (1600 $\mu\text{m}^2$ , comparable  
313 to the single shank of Neuropixels probes), distributing this displacement over many small elements has been  
314 shown (Skousen *et al.* 2011) to avoid deleterious tissue reactions.

315 An important objective was to improve co-registration of recording sites with meso-scale histological  
316 markers. We and others have previously attempted co-registration with  $\mu$ -opioid-receptor-defined striatal patches  
317 by observing tissue damage or gliosis produced by electrodes (White and Hiroi 1998), passing current to produce  
318 marker lesions (Berke *et al.* 2004; Friedman *et al.* 2015) or coating probes in lipophilic tracer dyes such as DiI  
319 (Fujisawa *et al.* 2008b). We have not found these approaches to be highly reliable and effective for identifying  
320 patch neurons – for example, dye coating is typically too uneven, while lesions destroy the essential  
321 immunochemical markers just where they are most needed. Some studies of patch neurons identified using

322 imaging have begun to appear (Bloem et al. 2017; Yoshizawa et al. 2018). However, our slice-in-place approach  
323 offers higher temporal resolution with less damage to nearby brain tissue.

324 We chose 300 $\mu$ m thick slabs for slice-in-place analysis. Thinner sections would include less of the  
325 recording zone and require more registration between sections, and increase the chance that short shank portions  
326 fall out of tissue during slicing. Thicker slabs would avoid these concerns, but are harder for antibodies to  
327 penetrate, and make microscopy more challenging due to increased light scattering. Scattering can be greatly  
328 reduced by tissue clearing (Chung and Deisseroth 2013; Ertürk *et al.* 2012; Hama *et al.* 2015) but we have found  
329 it is hard to avoid measurable shrinkage/expansion as the tissue is cleared, which impedes co-registration. Future  
330 improvements to our approach could use thicker slabs (or whole brains) together with enhanced clearing methods  
331 that avoid changes in tissue volume, and smaller antibodies (e.g. nanobodies; Perruchini *et al.* 2009) for more  
332 effective tissue penetration. The small size of the tips of the shanks might lend itself well to forming three-  
333 dimensional electrode arrangements, for example by stacking (Rios *et al.* 2016). If brain structures at different  
334 depths are targeted for simultaneous recording, the length of each shank and arrangement of can be chosen  
335 individually, and clusters of shanks can be precisely tailored to their targets.

336 Overall the cellular-scale silicon probes presented here are part of a new generation of devices for chronic  
337 monitoring of large neural populations (Chung *et al.* 2019; Hanson *et al.* 2019; Jun *et al.* 2017; Obaid *et al.* 2020).  
338 Their complementary geometry, small feature size, and the ability to achieve co-registration with histology make  
339 these probes suitable for addressing many outstanding questions in systems neuroscience.

#### 340 **Acknowledgements**

341 Probe fabrication was performed at the Lurie Nanofabrication Facility, a member of the National Nanotechnology  
342 Infrastructure Network, which is supported in part by the National Science Foundation. This work was supported  
343 by NIH BRAIN Initiative grants U01NS094375 and UF1NS107659, the University of Michigan, and the  
344 University of California San Francisco. We thank Michael Farries for assistance with GP recordings. Probes may  
345 be available in limited amounts upon request to the corresponding author.

#### 346 **References:**

347 Adam Y, Kim JJ, Lou S, Zhao Y, Xie ME, Brinks D, Wu H, Mostajo-Radji MA, Kheifets S, Parot V, Chettih S,  
348 Williams KJ, Gmeiner B, Farhi SL, Madisen L, Buchanan EK, Kinsella I, Zhou D, Paninski L, Harvey CD, Zeng H,  
349 Arlotta P, Campbell RE, Cohen AE. Voltage imaging and optogenetics reveal behaviour-dependent changes in  
350 hippocampal dynamics. *Nature* 569: 413–417, 2019.

351 Berényi A, Somogyvári Z, Nagy AJ, Roux L, Long JD, Fujisawa S, Stark E, Leonardo A, Harris TD, Buzsáki G.  
352 Large-scale, high-density (up to 512 channels) recording of local circuits in behaving animals. *J Neurophysiol* 111: 1132–  
353 1149, 2014.

354 Berke JD, Okatan M, Skurski J, Eichenbaum HB. Oscillatory entrainment of striatal neurons in freely moving rats.

- 355 *Neuron* 43: 883–896, 2004.
- 356 **Biran R, Martin DC, Tresco PA.** Neuronal cell loss accompanies the brain tissue response to chronically implanted silicon  
357 microelectrode arrays. *Exp Neurol* 195: 115–126, 2005.
- 358 **Bjornsson CS, Oh SJ, Al-Kofahi YA, Lim YJ, Smith KL, Turner JN, De S, Roysam B, Shain W, Kim SJ.** Effects of  
359 insertion conditions on tissue strain and vascular damage during neuroprosthetic device insertion. *J Neural Eng* 3: 196–207,  
360 2006.
- 361 **Blanche TJ, Spacek MA, Hetke JF, Swindale N V.** Polytrodes: High-density silicon electrode arrays for large-scale  
362 multiunit recording. *J Neurophysiol* 93: 2987–3000, 2005.
- 363 **Bloem B, Huda R, Sur M, Graybiel AM.** Two-photon imaging in mice shows striosomes and matrix have overlapping but  
364 differential reinforcement-related responses. *Elife* 6, 2017.
- 365 **Cai DJ, Aharoni D, Shuman T, Shobe J, Biane J, Song W, Wei B, Veshkini M, La-Vu M, Lou J, Flores SE, Kim I,  
366 Sano Y, Zhou M, Baumgaertel K, Lavi A, Kamata M, Tuszyński M, Mayford M, Golshani P, Silva AJ.** A shared neural  
367 ensemble links distinct contextual memories encoded close in time. *Nature* 534: 115–118, 2016.
- 368 **Chung JE, Joo HR, Fan JL, Liu DF, Barnett AH, Chen S, Geaghan-Breiner C, Karlsson MPM, Karlsson MPM, Lee  
369 KY, Liang H, Magland JF, Pebbles JA, Tooker AC, Greengard LF, Tolosa VM, Frank LM.** High-Density, Long-  
370 Lasting, and Multi-region Electrophysiological Recordings Using Polymer Electrode Arrays. *Neuron* 101: 21-31.e5, 2019.
- 371 **Chung K, Deisseroth K.** CLARITY for mapping the nervous system. *Nat Methods* 10: 508–513, 2013.
- 372 **Dai X, Hong G, Gao T, Lieber CM.** Mesh Nanoelectronics: Seamless Integration of Electronics with Tissues. *Acc Chem  
373 Res* 51: 309–318, 2018.
- 374 **Desban M, Kemel ML, Glowinski J, Gauchy C.** Spatial organization of patch and matrix compartments in the rat striatum.  
375 *Neuroscience* 57: 661–671, 1993.
- 376 **Du J, Blanche TJ, Harrison RR, Lester HA, Masmanidis SC.** Multiplexed, high density electrophysiology with  
377 nanofabricated neural probes. *PLoS One* 6, 2011.
- 378 **Ertürk A, Becker K, Jährling N, Mauch CP, Hojer CD, Egen JG, Hellal F, Bradke F, Sheng M, Dodt HU.** Three-  
379 dimensional imaging of solvent-cleared organs using 3DISCO. *Nat Protoc* 7: 1983–1995, 2012.
- 380 **Felix SH, Shah KG, Tolosa VM, Sheth HJ, Tooker AC, Delima TL, Jadhav SP, Frank LM, Pannu SS.** Insertion of  
381 flexible neural probes using rigid stiffeners attached with biodissolvable adhesive. *J Vis Exp* , 2013. doi:10.3791/50609.
- 382 **Friedman A, Homma D, Gibb LG, Amemori KI, Rubin SJ, Hood AS, Riad MH, Graybiel AM.** A corticostriatal path  
383 targeting striosomes controls decision-making under conflict. *Cell* 161: 1320–1333, 2015.
- 384 **Fujisawa S, Amarasingham A, Harrison MT, Buzsáki G.** Behavior-dependent short-term assembly dynamics in the

385 medial prefrontal cortex. *Nat Neurosci* 11: 823–833, 2008a.

386 **Garg AK, Li P, Rashid MS, Callaway EM.** Color and orientation are jointly coded and spatially organized in primate  
387 primary visual cortex. *Science* 364: 1275–1279, 2019.

388 **Graybiel AM, Ragsdale CW, Yoneoka ES, Elde RP.** An immunohistochemical study of enkephalins and other  
389 neuropeptides in the striatum of the cat with evidence that the opiate peptides are arranged to form mosaic patterns in register  
390 with the striosomal compartments visible by acetylcholinesterase stainin. *Neuroscience* 6, 1981.

391 **Guitchounts G, Markowitz JE, Liberti WA, Gardner TJ.** A carbon-fiber electrode array for long-term neural recording. *J*  
392 *Neural Eng* 10: 046016, 2013.

393 **Hama H, Hioki H, Namiki K, Hoshida T, Kurokawa H, Ishidate F, Kaneko T, Akagi T, Saito T, Saïdo T, Miyawaki A.**  
394 ScaleS: An optical clearing palette for biological imaging. *Nat Neurosci* 18: 1518–1529, 2015.

395 **Hanson T, Diaz-Botia C, Kharazia V, Maharbiz M, Sabes P.** The “sewing machine” for minimally invasive neural  
396 recording. *bioRxiv* 578542, 2019.

397 **Jun JJ, Steinmetz NA, Siegle JH, Denman DJ, Bauza M, Barbarits B, Lee AK, Anastassiou CA, Andrei A, Aydin Ç,**  
398 **Barbic M, Blanche TJ, Bonin V, Couto J, Dutta B, Gratiy SL, Gutnisky DA, Häusser M, Karsh B, Ledochowitsch P,**  
399 **Lopez CM, Mitelut C, Musa S, Okun M, Pachitariu M, Putzeys J, Rich PD, Rossant C, Sun WL, Svoboda K,**  
400 **Carandini M, Harris KD, Koch C, O’Keefe J, Harris TD.** Fully integrated silicon probes for high-density recording of  
401 neural activity. *Nature* 551: 232–236, 2017.

402 **Kita H, Kita ST.** The morphology of globus pallidus projection neurons in the rat: an intracellular staining study. *Brain Res*  
403 636: 308–319, 1994.

404 **Kozai TDY, Langhals NB, Patel PR, Deng X, Zhang H, Smith KL, Lahann J, Kotov NA, Kipke DR.** Ultrasmall  
405 implantable composite microelectrodes with bioactive surfaces for chronic neural interfaces. *Nat Mater* 11: 1065–1073,  
406 2012.

407 **Liu J.** Syringe Injectable Electronics. Springer, Cham, p. 65–93.

408 **Luan L, Wei X, Zhao Z, Siegel JJ, Potnis O, Tuppen CA, Lin S, Kazmi S, Fowler RA, Holloway S, Dunn AK,**  
409 **Chitwood RA, Xie C.** Ultraflexible nanoelectronic probes form reliable, glial scar-free neural integration. *Sci Adv* 3:  
410 e1601966, 2017.

411 **Merriam SME, Srivannavit O, Gulari MN, Wise KD.** A three-dimensional 64-site folded electrode array using planar  
412 fabrication. *J Microelectromechanical Syst* 20: 594–600, 2011.

413 **Michon F, Aarts A, Holzhammer T, Ruther P, Borghs G, McNaughton B, Kloosterman F.** Integration of silicon-based  
414 neural probes and micro-drive arrays for chronic recording of large populations of neurons in behaving animals. *J Neural*  
415 *Eng* 13, 2016.

416 **Mitz AR, Bartolo R, Saunders RC, Browning PG, Talbot T, Averbek BB.** High channel count single-unit recordings  
417 from nonhuman primate frontal cortex. *J Neurosci Methods* 289: 39–47, 2017.

418 **Musk E and Neuralink.** An Integrated Brain-Machine Interface Platform With Thousands of Channels. *J Med Internet Res*  
419 21: e16194, 2019.

420 **Obaid A, Hanna ME, Wu YW, Kollo M, Racz R, Angle MR, Müller J, Brackbill N, Wray W, Franke F, Chichilnisky**  
421 **EJ, Hierlemann A, Ding JB, Schaefer AT, Melosh NA.** Massively parallel microwire arrays integrated with CMOS chips  
422 for neural recording. *Sci Adv* 6: eaay2789, 2020.

423 **Pachitariu M, Steinmetz N, Kadir S, Carandini M, Kenneth D. H.** Kilosort: realtime spike-sorting for extracellular  
424 electrophysiology with hundreds of channels. *bioRxiv* 061481, 2016.

425 **Patel PR, Na K, Zhang H, Kozai TDYY, Kotov NA, Yoon E, Chestek CA.** Insertion of linear 8.4 µm diameter 16 channel  
426 carbon fiber electrode arrays for single unit recordings. *J Neural Eng* 12: 046009, 2015.

427 **Patel PR, Zhang H, Robbins MT, Nofar JB, Marshall SP, Kobylarek MJ, Kozai TDY, Kotov NA, Chestek CA.**  
428 Chronic in vivo stability assessment of carbon fiber microelectrode arrays. *J Neural Eng* 13: 066002, 2016.

429 **Perruchini C, Pecorari F, Bourgeois JP, Duyckaerts C, Rougeon F, Lafaye P.** Llama VHH antibody fragments against  
430 GFAP: Better diffusion in fixed tissues than classical monoclonal antibodies. *Acta Neuropathol* 118: 685–695, 2009.

431 **Potter KA, Buck AC, Self WK, Capadona JR.** Stab injury and device implantation within the brain results in inversely  
432 multiphasic neuroinflammatory and neurodegenerative responses. *J Neural Eng* 9: 046020, 2012.

433 **Prasad A, Xue QS, Sankar V, Nishida T, Shaw G, Streit WJ, Sanchez JC.** Comprehensive characterization and failure  
434 modes of tungsten microwire arrays in chronic neural implants. *J Neural Eng* 9: 056015, 2012.

435 **Rios G, Lubenov E V., Chi D, Roukes ML, Siapas AG.** Nanofabricated Neural Probes for Dense 3-D Recordings of Brain  
436 Activity. *Nano Lett* 16: 6857–6862, 2016.

437 **Saxena T, Karumbaiah L, Gaupp EA, Patkar R, Patil K, Betancur M, Stanley GB, Bellamkonda R V.** The impact of  
438 chronic blood-brain barrier breach on intracortical electrode function. *Biomaterials* 34: 4703–4713, 2013.

439 **Scholvin J, Kinney JP, Bernstein JG, Moore-Kochlacs C, Kopell N, Fonstad CG, Boyden ES.** Close-packed silicon  
440 microelectrodes for scalable spatially oversampled neural recording. *IEEE Trans Biomed Eng* 63: 120–130, 2016.

441 **Schwarz DA, Lebedev MA, Hanson TL, Dimitrov DF, Lehew G, Meloy J, Rajangam S, Subramanian V, Ifft PJ, Li Z,**  
442 **Ramakrishnan A, Tate A, Zhuang KZ, Nicolelis MAL.** Chronic, wireless recordings of large-scale brain activity in freely  
443 moving rhesus monkeys. *Nat Methods* 11: 670–676, 2014.

444 **Shobe JL, Claar LD, Parhami S, Bakhurin KI, Masmanidis SC.** Brain activity mapping at multiple scales with silicon  
445 microprobes containing 1,024 electrodes. *J Neurophysiol* 114: 2043–2052, 2015.

- 446 **Skousen JL, Merriam SME, Srivannavit O, Perlin G, Wise KD, Tresco PA.** Reducing surface area while maintaining  
447 implant penetrating profile lowers the brain foreign body response to chronically implanted planar silicon microelectrode  
448 arrays. In: *Progress in Brain Research*. Elsevier, p. 167–180.
- 449 **Staudt T, Lang MC, Medda R, Engelhardt J, Hell SW.** 2,2'-Thiodiethanol: A new water soluble mounting medium for  
450 high resolution optical microscopy. *Microsc Res Tech* 70: 1–9, 2007.
- 451 **Straub C, Saulnier JL, Bègue A, Feng DD, Huang KW, Sabatini BL.** Principles of Synaptic Organization of GABAergic  
452 Interneurons in the Striatum. *Neuron* 92: 84–92, 2016.
- 453 **Tanghe SJ, Najafi K, Wise KD.** A planar IrO multichannel stimulating electrode for use in neural prostheses. *Sensors*  
454 *Actuators B Chem* 1: 464–467, 1990.
- 455 **Wang S, Garakoui SK, Chun H, Salinas DG, Sijbers W, Putzeys J, Martens E, Craninckx J, Van Helleputte N, Lopez**  
456 **CM.** A Compact Quad-Shank CMOS Neural Probe With 5,120 Addressable Recording Sites and 384 Fully Differential  
457 Parallel Channels. *IEEE Trans Biomed Circuits Syst* 13: 1625–1634, 2019.
- 458 **White NM. & Hiroi N.** Preferential localization of self-stimulation sites in striosomes/patches in the rat striatum. *Proc. Natl.*  
459 *Acad. Sci. U. S. A.* 95, 6486–6491, 1998.
- 460 **Wiltchko AB, Gage GJ, Berke JD.** Wavelet filtering before spike detection preserves waveform shape and enhances  
461 single-unit discrimination. *J Neurosci Methods* 173: 34–40, 2008.
- 462 **Winslow BD, Tresco PA.** Quantitative analysis of the tissue response to chronically implanted microwire electrodes in rat  
463 cortex. *Biomaterials* 31: 1558–1567, 2010.
- 464 **Wu F, Stark E, Ku PC, Wise KD, Buzsáki G, Yoon E.** Monolithically Integrated  $\mu$ LEDs on Silicon Neural Probes for  
465 High-Resolution Optogenetic Studies in Behaving Animals. *Neuron* 88: 1136–148, 2015.
- 466 **Xie C, Liu J, Fu T-MM, Dai X, Zhou W, Lieber CM.** Three-dimensional macroporous nanoelectronic networks as  
467 minimally invasive brain probes. *Nat Mater* 14: 1286–1292, 2015.
- 468 **Yoshizawa T, Ito M, Doya K.** Reward-predictive neural activities in striatal striosome compartments. *eNeuro* 5, 2018.

469  
470

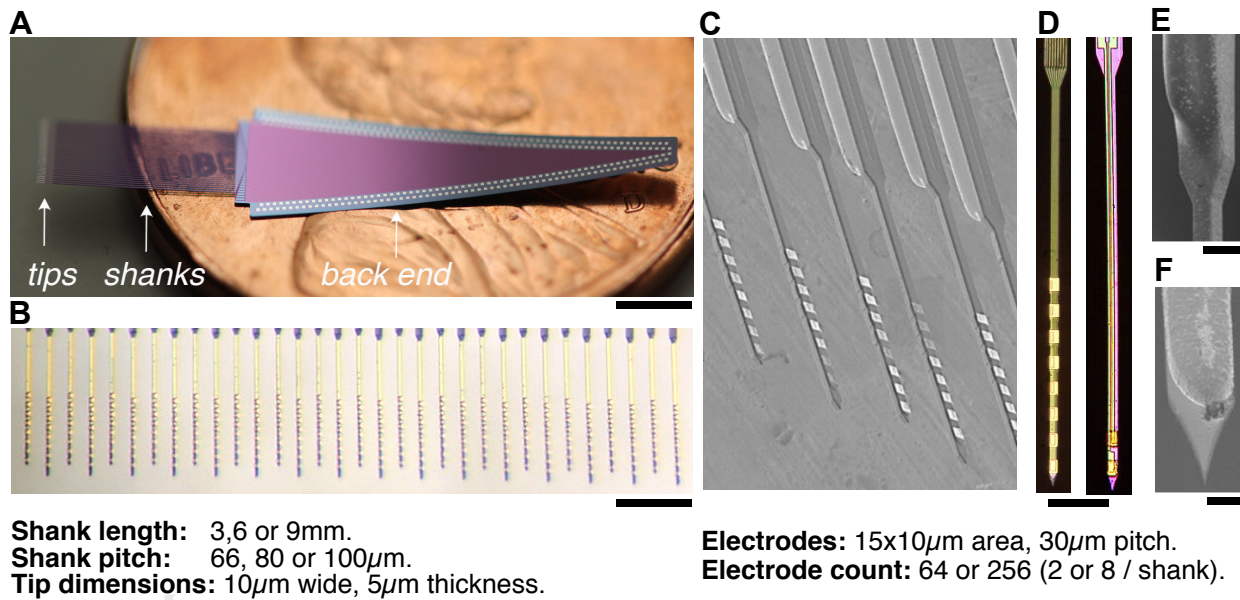


**Figure 1: Silicon probes with cellular-scale tips.** **A**, 256-channel probe (6mm shank version), on penny for scale. Scale: 3mm. **B**, Close-up of tip portion showing 32 shanks, each with 8 electrodes. Scale: 200 $\mu$ m. **C**, Electron micrograph of probe tips, showing electrodes. **D**, Comparison of shanks with 8 electrodes (left; in 256 channel probes) and 2 electrodes (right; in 64 channel probes). Scale: 50 $\mu$ m. **E**, Smooth transition to stiffener-reinforced upper section. Scale: 10 $\mu$ m. **F**, Sharpened tip. Scale: 5 $\mu$ m.

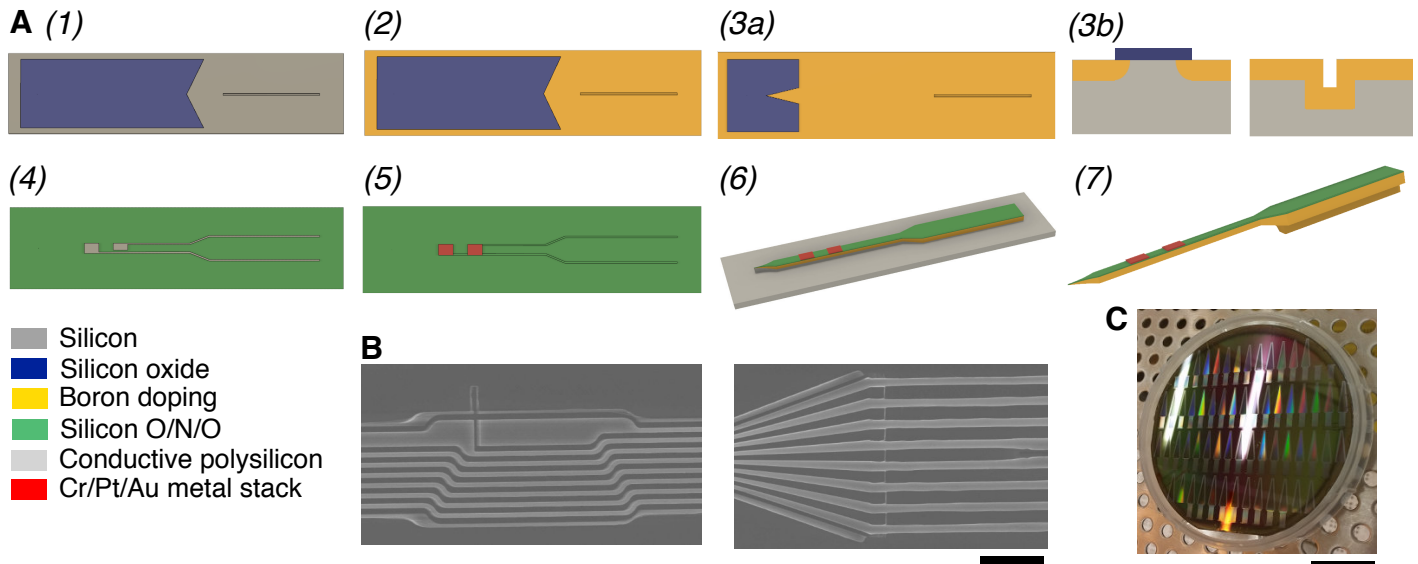


**Figure 2: A**, Main steps and materials of the nanofabrication process flow: (1) Grow and pattern silicon oxide to form a masking layer. Etch trench using deep reactive ion etching (DRIE) for stiffeners. (2) Diffuse boron into silicon in places that were not masked. (3) Remove the mask except for a small section around the tip ends. Perform a second boron diffusion to define tip thickness (3a top view, 3b side view). (4) Deposit stack of electrically insulating silicon oxide, silicon nitride and silicon oxide. Deposit layer of electrically conductive polysilicon and pattern to form interconnects. (5) Deposit another insulator stack (as before). Etch vias, sputter Cr/Pt/Au and pattern via lift-off to form bonding pads and electrodes. (6) Etch probe outline using DRIE. (7) Etch undoped silicon with ethylene diamine pyrocatechol (EDP). **B**, Close-up of polysilicon interconnects shaped with e-beam lithography (left) and transition to stepper patterning (right). Scale:  $5\mu\text{m}$ . **C**, Completed wafer. For handling and protection of the fine tips the devices remain attached to the wafer frame by small tabs. Scale: 2cm.

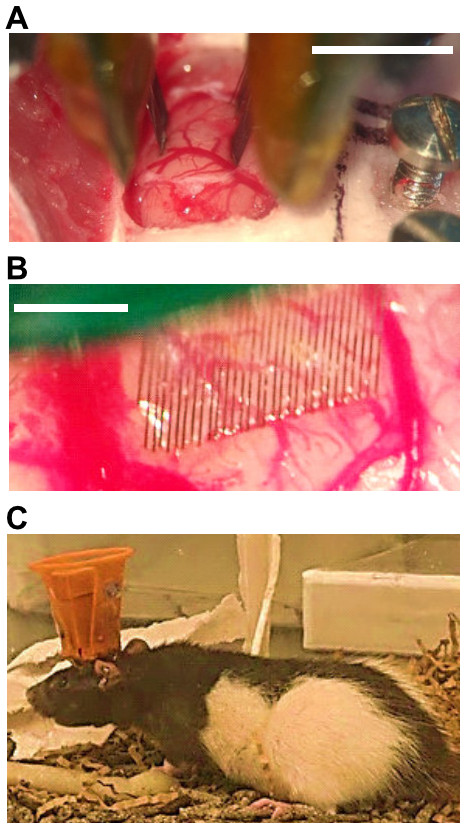
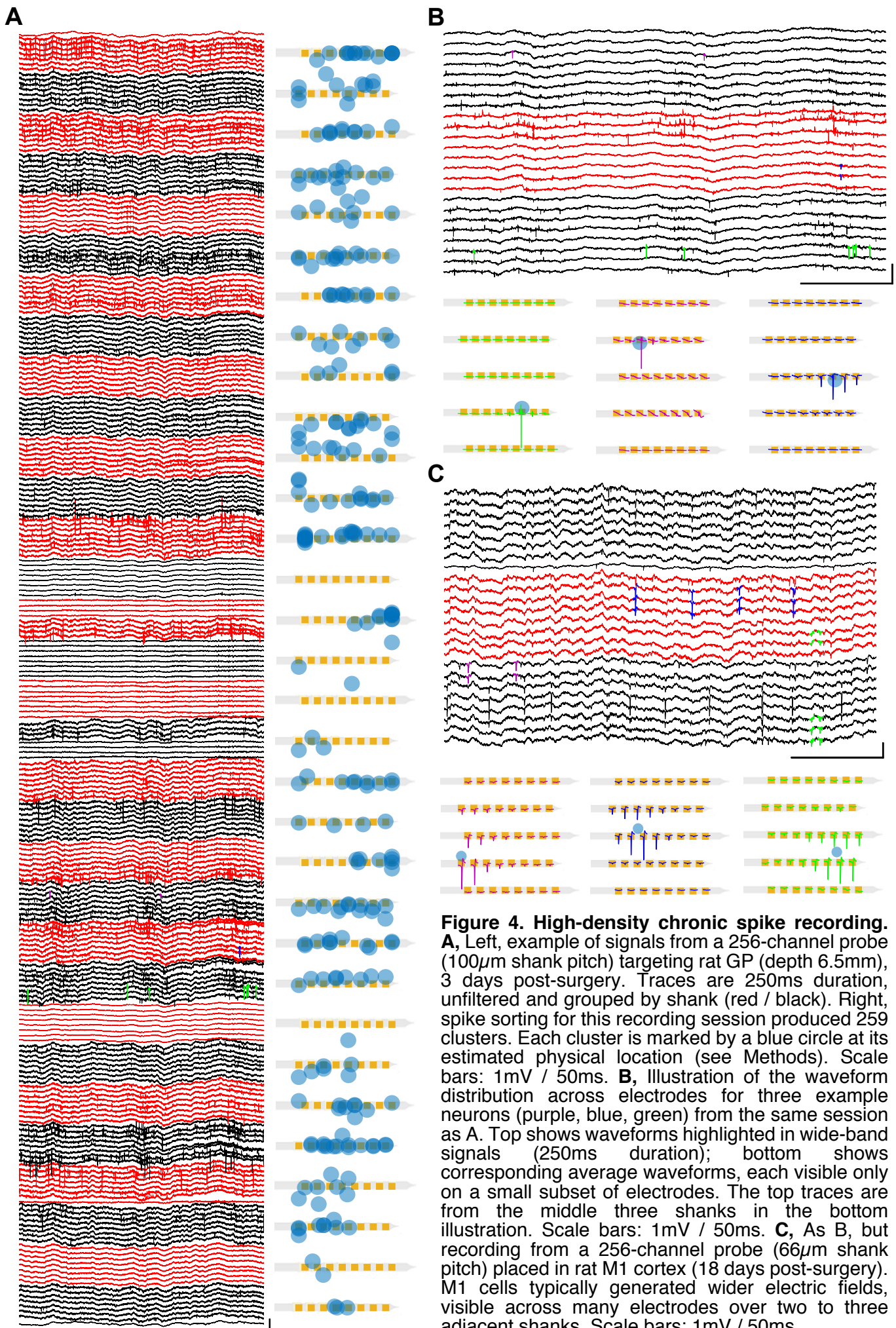


**Figure 3: Probe insertion.**

**A**, Two devices (6mm, 9mm lengths) being implanted into the same hemisphere for simultaneous recording from motor cortex and striatum. Scale: 2mm.

**B**, Device with  $66\mu\text{m}$  pitch between shanks (and 3mm length) being inserted 1.5mm deep into motor cortex. Scale: 1mm.

**C**, Rat after recovery, with 256 channel implanted device connected to 2 x 128 channel Intan headstages within a 3D-printed enclosure.



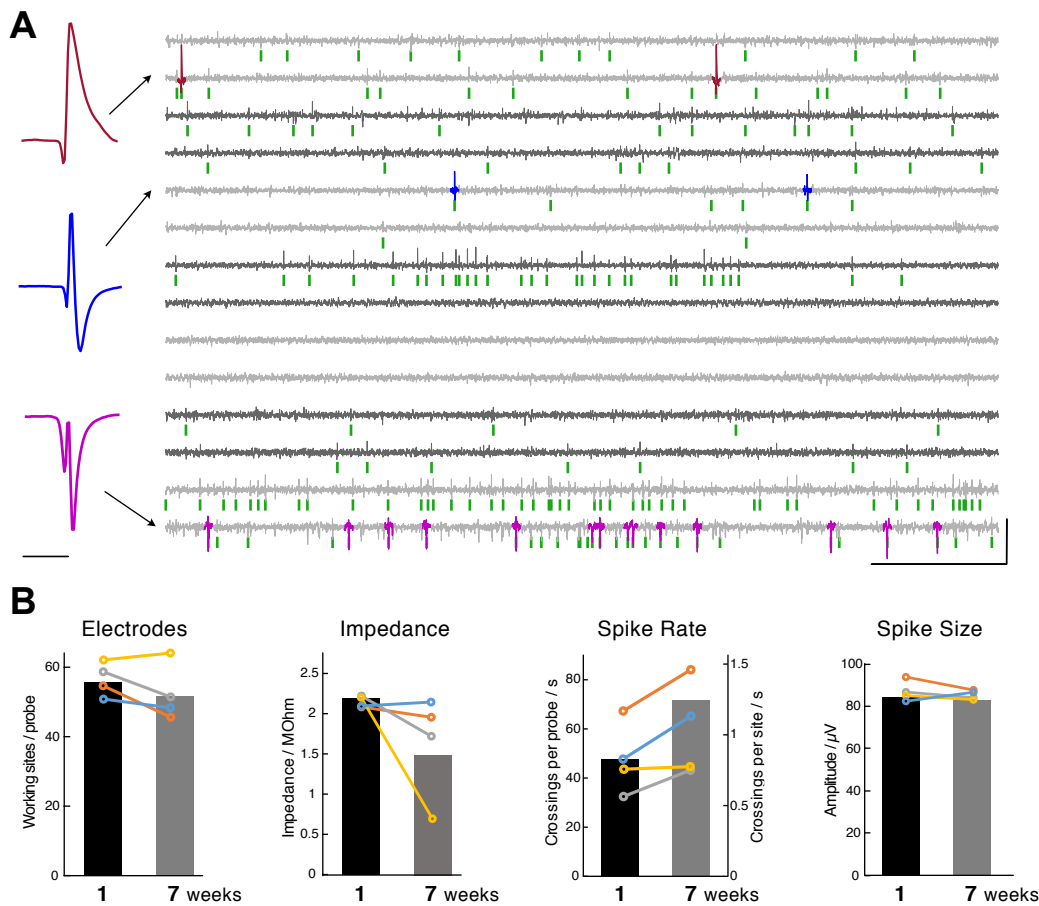


**Figure 5: Cellular-scale silicon probes record spikes for many weeks. A,** Example recording from a 64-channel probe, 139 days after implantation into dorsal striatum (250ms shown). Signals are high-pass filtered and color-coded by shank (alternating light and dark gray; 7 shanks shown out of 32 total). Examples of spikes from large units are highlighted in color, with the corresponding average waveforms shown at left (peak-valley ranges: brown 300 $\mu$ V, blue 186 $\mu$ V, magenta 190 $\mu$ V). Green marks below signals indicate all detected spike events (threshold of 6 x median absolute deviation). Scales (left): 1ms; (right) 300 $\mu$ V / 50ms. **B,** Performance metrics comparing 1 week post-implant (6-7 days) with 7 weeks (49-50 days). Same implant type, same 6 x M.A.D. event threshold as in (A). Colored lines indicate individual animals (n=4 probes, 256 sites total), black and grey bars indicate probe means (in left-most plot) or means for working electrodes (other plots).

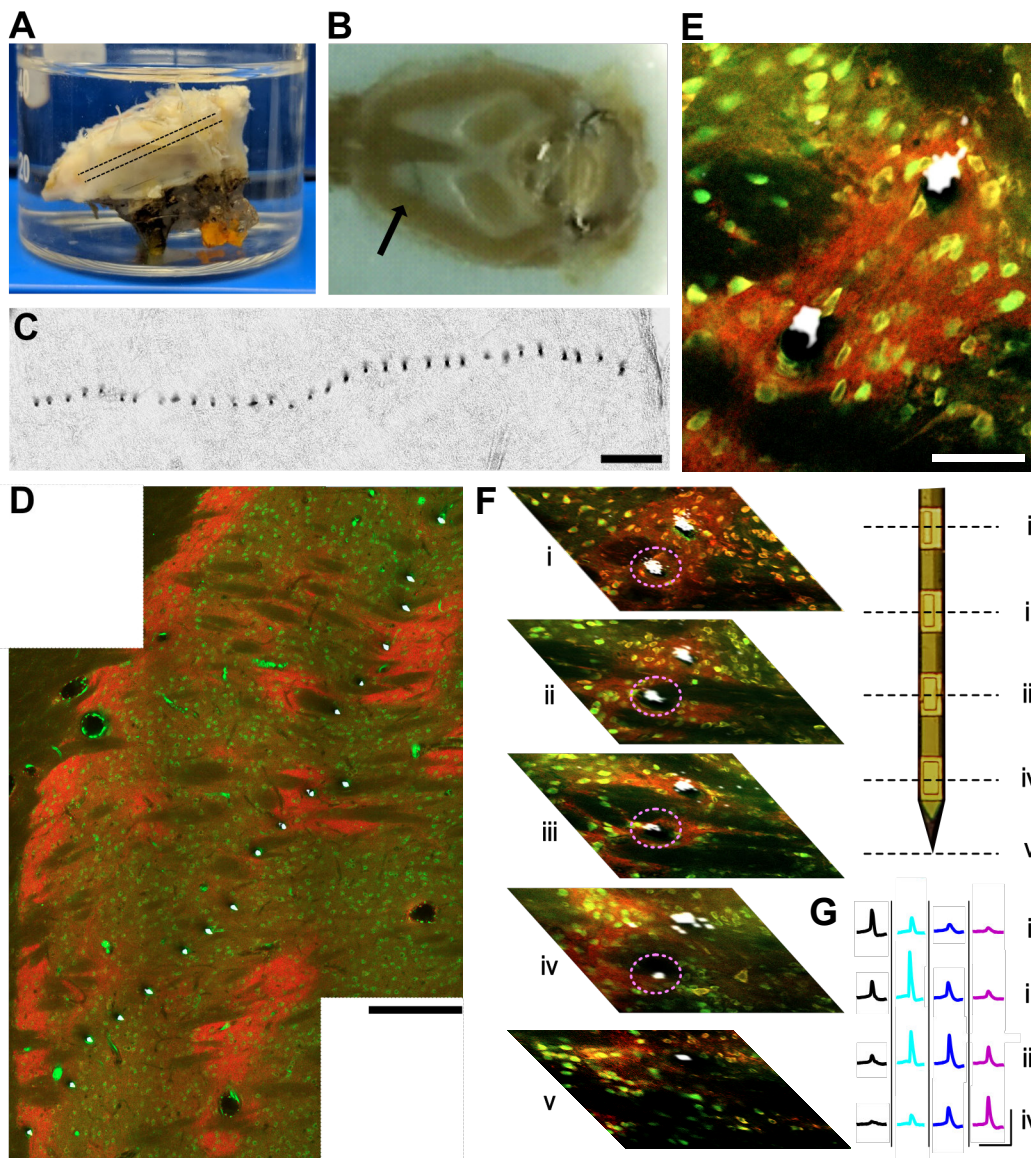


**Figure 6: Slice-in-place approach for precise localization of electrodes within brain circuits.** **A**, Decalcification of the skull (shown upside-down) after removal of superficial tissue. The dashed line indicates the plane and thickness of slices. **B**, Skull and brain are sliced together, ventral to dorsal, with the probes *in situ*. Faint gray line (arrow) is the row of shanks. **C**, Example of probe tips within striatum (brightfield image), at about 4.3 mm depth. Scale: 400 $\mu$ m. **D**, Shank tips (white; inverted, thresholded brightfield image) superimposed on immunofluorescence imaging of neurons (NeuN, green) and striatal patches ( $\mu$ -opioid receptors, red) in the same plane. Scale: 200 $\mu$ m. **E**, Close-up histology from a chronic striatum implant (35 days survival post-surgery; staining as in D). Patch neurons are visible immediately adjacent to the shanks at lower right. Scale: 50 $\mu$ m. **F**, Stack of confocal images for the lower sections of the two shanks shown in E. Depths correspond to electrode locations and probe tip for one shank (circled; corresponding schematic on upper right side). Scale: 50 $\mu$ m. **G**, Depth profiles for the average waveforms of four example single-units (columns) recorded on day 35 from the same four electrodes as F. Scale: 100 $\mu$ V, 4ms.